Classification:

Biological Science – Environmental Sciences

Title:

Reducing uncertainties in decadal variability of the global carbon budget with multiple data sets

Wei Li[a,1], Philippe Ciais[a], Yilong Wang[a], Shushi Peng[a], Gregoire Broquet[a], Ashley P. Ballantyne[b], Josep G. Canadell[c], Leila A. Cooper[b], Pierre Friedlingstein[d], Corinne Le Quéré[e], Ranga B. Myneni[f], Glen Peters[g], Shilong Piao[h], Julia Pongratz[i]

Authors from A.P.B. onward are in the alphabetical order of last names.

[a]Laboratoire des Sciences du Climat et de l'Environnement, LSCE/IPSL, CEA-CNRS-UVSQ, Université Paris-Saclay, F-91191 Gif-sur-Yvette, France

[b]Department of Ecosystem and Conservation Science, University of Montana, Missoula, MT, USA

[c]Global Carbon Project, CSIRO Oceans and Atmosphere, GPO Box 3023, Canberra, ACT 2601, Australia

[d]College of Engineering, Mathematics and Physical Sciences, University of Exeter, Exeter EX4 4QF, UK

[e]Tyndall Centre for Climate Change Research, University of East Anglia, Norwich Research Park, Norwich NR4 7TJ, UK

[f]Department of Earth and Environment, Boston University, Boston, MA 02215, USA

[g]Center for International Climate and Environmental Research – Oslo (CICERO), Oslo, Norway

[h]Department of Ecology, College of Urban and Environmental Sciences, Peking University, Beijing 100871, China

[i]Max Planck Institute for Meteorology, Hamburg, Germany

[1]Corresponding author phone: 0033-6-58276925; email: wei.li@lsce.ipsl.fr

Keywords:

global carbon budget; decadal variations; Bayesian fusion; GPP

Abstract

Conventional calculations of the global carbon budget infer the land sink as a residual between emissions, atmospheric accumulation and the ocean sink. Thus, the land sink accumulates the errors from the other flux terms and bears the largest uncertainty. Here, we present a Bayesian fusion approach that combines multiple observations in different carbon reservoirs to optimize the land (B) and ocean (O) carbon sinks, land-use change emissions (L), and indirectly fossil fuel emissions (F) from 1980 to 2014. Compared to the conventional approach, Bayesian optimization decreases the uncertainties in B by 41% and in O by 47%. The L uncertainty decreases by 46% whereas F uncertainty marginally improves through the knowledge of all the other terms. Both ocean and net land uptake (B+L) rates have positive trends of 28±8 and 43±17 Tg C yr^{-2} since 1980, respectively. We explore the possibility of separating the net land flux into gross primary production (GPP), terrestrial ecosystem respiration (TER) and fire emissions by using proxies for GPP and TER trends, namely satellite vegetation greenness and the time-series from a global database of field-scale soil respiration. Between 1980 and 1994, GPP grew faster than TER, causing an increasing net land sink. After 2000, both GPP and TER growth stalled, leading to the maintenance of the land sink. This suggests that a different regime of GPP and TER trends explains the land sink after 2000. Our Bayesian fusion of multiple observations reduces uncertainties thereby allowing us to isolate important variability in global carbon cycle processes.

Significance Statement

The conventional approach of calculating the global carbon budget makes the land sink the most uncertain of all budget terms. This is because rather than being constrained by observations it is inferred as a residual in the budget equation. Here, we overcome this limitation by performing a Bayesian fusion of different available observation-based estimates of decadal carbon fluxes. This approach reduces the uncertainty in the land sink by 41% and in the ocean sink by 47%. These results are significant because they give unprecedented confidence in the role of the increasing land sink in regulating atmospheric CO_2, and shed light on the past decadal trend where the land sink continued to grow despite plant carbon uptake having stalled.

The land and ocean carbon sinks provide a vital ecosystem service by absorbing on average about 55% of anthropogenic CO_2 emissions from fossil fuel combustion and land-use change. Research has focused on understanding the relationships between year-to-year variability in carbon sinks and climate (1, 2), as well as the long term trend over the full instrumental period of CO_2 monitoring at the Mauna Loa station (3). Quasi-decadal variations of emissions and sinks have received comparatively less attention. Yet, significant climate variation occurs at this specific time scale (4). Since 1980, the variable occurrence of different ENSO events, two large volcanic eruptions (El Chichón and Pinatubo) and the recent slow-down of land surface warming (hiatus) have modulated the strength of natural carbon sinks. There are also decadal-scale changes in the rate at which human activities perturb the natural carbon cycle, in particular the recent acceleration of fossil fuel and cement emissions in the 2000s (5) and the slow-down in global land-use change emissions (LUC) in the mid-2000s, which appears to be partly driven by reduced deforestation in Brazil (6).

Here, we provide a data-driven assessment of global CO_2 emissions and sinks at 5-year intervals for the period of 1980-2014. We use a new Bayesian fusion approach whereby different data-streams of ocean and land uptake, LUC emissions, are optimally combined, and their uncertainty reduced from prior knowledge. This approach estimates the land sink constrained by data, which is a major improvement over the "conventional" method for calculating the global carbon budget by Ciais et al. (7) and Le Quéré et al. (8), hereafter LQ15, where the unknown land sink was determined as a residual from the other components (emissions, atmospheric increase, ocean uptake). Most of the data-streams used in this analysis start in 1980, and about half of them give decadal mean values of natural sinks and thus do not allow us to tackle the reconstruction of interannual variability. Our choice of applying a Bayesian fusion approach to optimize 5-year average component fluxes of the global carbon budget is therefore a compromise that maximizes the use of available observations of decadal average fluxes.

The principle of the Bayesian fusion approach is to combine an *a priori* imperfect knowledge of fluxes with observations and their uncertainties to infer optimized estimates of fluxes. Here, we define *a priori* values of terms in the global carbon budget that are not from observations. Specifically, we set prior fossil fuel and cement emissions (F) from inventories and the simulated land, ocean and land-use change carbon fluxes from process-based models (Table S1). Observational data sets independent from those prior values are applied to constrain land-use change emissions (L), the ocean uptake of anthropogenic CO_2 (O), the land-biosphere sink (B) in ecosystems not affected by land-use change, and the net land flux (B+L) (Table S2). A more uncertain attempt to extend the Bayesian optimization approach is proposed, where the net land flux is decomposed into three gross carbon fluxes: Gross Primary Production (GPP), Terrestrial Ecosystem Respiration (TER) and fire emissions (FR). Here the trends of GPP and TER are only indirectly constrained by the proxies of satellite-based vegetation greenness trends for GPP and of in-situ soil respiration data for TER.

Results

In the optimization of the global carbon budget (Opt-A, Fig. 1), the prior value of F and its uncertainty (Table S1) were defined from the mean value and the range of different emission inventories, namely from CDIAC (9), IEA (10), EDGAR (11) and BP (12) (Methods). These inventories are not treated as direct observations of emissions, and there is currently no independent observation to verify F. The prior values of O are from seven ocean biogeochemistry models (8), and the prior values of B are from the nine TRENDY land carbon models (13) (Methods). These prior values from state-of-the-art models are without direct observational constraints. The prior estimates of L are derived from the difference of simulated land carbon fluxes with and without LUC in the TRENDY carbon models (13). All fluxes are defined as positive if CO_2 is lost to the atmosphere by the land or the ocean reservoir. Uncertainties in the prior estimates of 5-yearly O, B and L, are set to the maximum between those reported by LQ15 and the standard deviations across models. All uncertainties here refer to 1-σ Gaussian errors. In this context, the prior uncertainties are 0.5 for O, 0.9 for B and 0.8 Pg C yr^{-1} for L, thus not smaller than the values of 0.5, 0.8 and 0.5 Pg C yr^{-1} from LQ15. It is important that the prior uncertainties are not too small, so that adding observations can adjust and constrain the sought fluxes.

Several independent data-streams, each with their specific uncertainty and temporal resolution (Fig. S1, Table S2), are combined in the Bayesian optimization with the above prior knowledge. These data-streams are: 1) the atmospheric CO_2 growth rate (CGR) from the NOAA/ESRL atmospheric network (14) which constrains the sum of all fluxes and is determined very accurately from more than 60 monitoring stations; 2) the atmospheric 5-year mean (negative) growth rate of O_2/N_2 in the atmosphere from the Scripps O_2 Program (15) which relates to the combined effect of B+L and F changes, while being insensitive to changes in O (note that O_2/N_2 has a negative trend in the atmosphere); 3) a set of yearly mean observation-based estimates of O from shipboard partial pressure of CO_2 surveys corrected for natural outgassing (16, 17) and decadal-mean observations of O from inventories of carbon change in the ocean (18–20); 4) ten-year mean estimates of B from a global synthesis of changes in forest carbon stocks (21) and inventory-based land carbon storage change from the RECCAP publications (Table S3); 5) decadal mean B+L based on microwave remote sensing of Vegetation Optical Depth (22); 6) five-year mean LUC emissions from two independent bookkeeping approaches constrained by observed carbon stocks (23, 24) and from the RECCAP publications (Table S3). The uncertainties in each data-stream are either derived directly from the original publications (when reported) or estimated from expert judgments (details in Table S2). The optimization is performed for seven consecutive 5-year windows between 1980 and 2014.

In the Bayesian optimization, observations that describe mean fluxes during intervals longer than 5-years are still useful to infer 5-yearly fluxes. For example, the mean ocean sink observation for the 1990s (19) constrains the mean 5-yearly O during 1990-1999, while other independent observations (O_2/N_2 and CGR) help to further separate O values between 1990-1994 and 1995-1999. Despite no direct observation of F, this flux is found to be slightly improved in the Bayesian fusion, through knowledge of the other terms, and because the sum of all fluxes is very well constrained from CGR observations (Methods). We are aware that some observation-based land sink estimates have systematic errors in the way they are included in the optimization. In particular, the estimate of B from ref. (21) is only for forests and ignores other biomes. However, the RECCAP studies (25–27) and other estimates (21, 22) of the carbon flux in non-forest biomes suggest that the forest sink alone accounts for most of the global land sink B.

The improved global budget of anthropogenic CO_2 in Opt-A is shown in Fig. 2, and all data are given in Table S1. After optimization, the *a posteriori* uncertainty in each flux is reduced. Compared to the conventional method applied by LQ15 and IPCC-AR5 (7), uncertainties in B and O are reduced by 41% and 47% in this study. In the Bayesian data fusion, the land sink is no longer solely inferred as a residual that accumulates uncertainties from all other terms, and it exhibits a large reduction in uncertainty. The uncertainty in L decreases by 46% but the uncertainty in F is marginally improved (by 2%) through the indirect constraints of other terms. In the absence of direct constraint on F, this small reduction in the F uncertainties compared to LQ15 and IPCC-AR5 (7) is also because we use multiple emission inventories (while LQ15 and IPCC-AR5 (7) only used CDIAC (9)) and start at relatively higher prior uncertainties in F (Table S1) than in LQ15. Despite their improved (smaller) uncertainties, the 5-year mean fluxes shown in Table S1 (Opt-A) do not differ statistically in their mean values from LQ15. This indicates that each flux of the Bayesian carbon budget is fully consistent with LQ15 even though we used an array of data with different measurement methods and with uncertainties estimated in different ways. Specifically, we obtain emissions from fossil fuel burning and cement production that are smaller than LQ15 by 0.24±0.16 Pg C yr^{-1} during 1980-1999 and 2005-2014 (Fig. 2), and higher by 0.14 Pg C yr^{-1} during 2000-2004. A downward revision of global F during 1980-1999 is consistent with the correction of the emissions for China based on evidence of the lower carbon content for coal burned in that country (28). Compared to LQ15, the optimized ocean sink during 2000-2004 is larger by 0.16 Pg C yr^{-1} but lower by 0.20±0.12 Pg C yr^{-1} during all the other periods. In the past decade (2005-2014), both ocean sink and land sink from our optimization are smaller than LQ15. The optimized fluxes of L are similar to or lower than those from LQ15. The trend of F for the seven 5-year periods is positive (p = 0.007), with a probability of a positive trend for O and B+L of 93%; the trend of B or L individually is not significant for (p = 0.23 and 0.13). The increasing rate of O and B+L are 28±8 and 43±17 Tg C yr^{-2} since 1980, respectively. Similar significantly positive trends were also found in the 5-year mean O and B+L between 1980 and 2014 calculated from the yearly budget updated by LQ15 (Fig. S2). Given the robustness of O inferred by Opt-A (see also Fig. S3), and in view of the many observations constraining this flux, there is a high confidence that the ocean sink has been increasing over time since 1980. The land sink from Opt-A is less variable between different 5-year periods than in LQ15 (Fig. S2). But the ocean sink is more variable, with a standard deviation of 0.36 Pg C yr^{-1} compared to 0.29 Pg C yr^{-1} by LQ15 (standard deviations across the seven periods analyzed).

From 1980 to 2014, the average fractions of F+L emission re-absorbed by the land and ocean carbon reservoirs are 29 ±6% and 26 ±2%, respectively. The ratios of both O and B to F+L emission do not exhibit any significant trends (p > 0.05, Fig. S4). Even with their reduced uncertainty in this study compared to LQ15, the variability of O and B between 5-year intervals prevents us from assessing the very small trends in their ratios to emissions. Similarly, we found no significant trend in the ratio of O or B to fossil fuel emission (F). The larger variability of the B-to-(F+L) ratios compared to the O-to-(F+L) ones (Fig. S4) suggests that the efficiency of the land sink at absorbing emissions is more variable than that of the ocean sink. For instance, during the period that followed the cooling from the Pinatubo eruption in 1990-1994 (29–31), the B-to-

(F+L) ratio increased by 41% above its long-term mean. This ratio was also higher than normal during 2005-2009, possibly due to the absence of El Niño and to the occurrence of a cooler and wetter La Niña event in 2008-2009 manifested by lower than normal CGR (3).

A second more exploratory optimization called Opt-B was attempted to further decompose changes in the net land carbon flux (B+L) into changes of gross fluxes of GPP, TER and FR. This second optimization (Fig. S5) uses observations to constrain the equation B + L = GPP + TER + FR, and fire emissions, and proxies to constrain changes of GPP and TER on 5-year successive intervals. The prior values of GPP, TER and FR are from the TRENDY land carbon models as in Opt-A (Methods, Table S1) (13). The data constraints on GPP and TER included in Opt-B (Table S2) are less stringent than those used for net fluxes in Opt-A because there are only indirect proxies of these fluxes. Namely, we used: 1) the decadal mean value of GPP during 2000-2009 derived from MODIS satellite observations (32) and from a data-driven product using both satellite and flux tower measurements (33); 2) a proxy of the GPP trend, given by the trend of satellite global leaf area index (LAI) since 1982 (yearly average of three LAI data sets (34–36)); 3) an indirect proxy of the global TER trend from the global trend observed in long-term field-scale soil respiration measurements (37). For fire emissions, we used 5-year mean values from three inventory- or satellite-based products (38–40). Only the decadal mean GPP from ref. (33) during 2000-2009 is used and not the trend of this GPP data-product, because this trend has been reported to be possibly underestimated (41).

The results of Opt-B are consistent with Opt-A for the net fluxes, which is not surprising because both optimizations share the same constraints for the net fluxes (Fig. S6). The optimized 5-year mean GPP and TER estimates are lower by about 10 Pg C yr^{-1} than their prior values (Fig. 3a), giving a best value of GPP = -127 ±8 Pg C yr^{-1} and TER = 124 ±8 Pg C yr^{-1}. The optimized fire emission (FR) is 2.3 Pg C yr^{-1} during 1980-2014, with a variability of 0.29 Pg yr^{-1} across the different 5-year periods (Fig. 3b). Compared with the prior value, FR decreases after optimization in all the seven 5-year periods, and its uncertainties are reduced by 54% from the prior (Fig. 3b). The reductions in both mean values and uncertainties of FR are mainly a result of the constraints of three inventory- and satellite-based fire emission data sets (38–40) (Tables S1 and S2).

In Opt-B, 5-year GPP and TER are found to increase from 1980 to 2000 (Fig. 3a). After 2000, a different regime is found: the growth in GPP stalled, but TER did not increase either, so that a net land sink was maintained (Fig. 3a, Table S1). The proxy data for GPP trends and TER trends used as observational constraints are sufficient in Opt-B to change the sign of the prior trends after 2000. The break point change in the trend of GPP and TER after 2000 is found to be more robust than the mean values of these fluxes, across a series of sensitivity tests (Methods, Figure S7). The GPP trend changed from 1.4 ±0.56 before 2000 to -0.026 ±0.10 Pg C yr^{-2} after 2000, and similarly, the TER trend decreased from 1.3 ±0.54 to -0.31 ±0.17 Pg C yr^{-2}. This reduction in the positive trend of GPP and TER after 2000 was not present in the prior from TRENDY models, where GPP and TER persistently increase during the last 35 years (13) (Fig. 3a). In Opt-B, the inferred stalling of growth in GPP is constrained by the stalling of global satellite LAI trend (consistent across three satellite LAI products (34–36)). Yet, it should not be over-interpreted since a stalled LAI is no proof of a stalled GPP because the light-use efficiency of plant canopies might have continued to increase while their fraction of intercepted solar radiation (directly related to LAI) may have stalled.

Discussion

The Bayesian approach used in this study provides the most robust estimate to date of the strength and evolution of the land sink and provides hints about how gross fluxes may have changed to cause this sink. The trend of 5-year mean GPP and TER reflect both decadal climate variability and long-term drivers such as the increasing concentration of CO_2, nitrogen deposition and land management. During 1990-1994, the five-year period within which the Pinatubo eruption occurred, we infer from Opt-B that GPP was abnormally high relative to TER (Fig. 3a, Table S1). This result supports the conclusions of previous studies that a positive effect on GPP occurred due to the increased fraction of diffuse light produced by volcanic aerosols (42) and TER was suppressed due to the cooling that followed the eruption (29). The stalled TER since 2000-2004 may reflect the effect of a slow-down soil carbon decomposition in response to the winter cooling of northern lands (43). It is not possible with our global approach to infer which region was responsible for the stalling of GPP and TER after 2000. Possible explanations for the recent stalling of global GPP could involve either emerging biogeochemical limitations (e.g., reduced nitrogen deposition in some regions, or emerging nutrient limitations elsewhere (44, 45)) or the slower warming at high latitudes resulting in a slower photosynthetic enhancement and lengthening of the growing season. Combining spatially explicit observations to constrain process-based carbon cycle models, as done e.g., in carbon cycle data assimilation systems (46, 47) should provide more insights about the regional processes and explain why GPP and TER have stalled in the 2000s. If the driver of the GPP stalling proves not to be the slower warming of the northern hemisphere after 2000, and should high warming rates resume in the coming decade, then TER would increase while GPP remains stalled. This combination is expected to strongly reduce the sink strength of land ecosystems, and would require stronger mitigation of anthropogenic emissions to keep to the climate stabilization pathway of 2°C recently agreed by 187 nations (48).

Acknowledgements

This paper builds on an analysis started by the late Michael R. Raupach and is a contribution to the work of the Global Carbon Project to understand and better constrain the human perturbation of the carbon budget. We thank Alessandro Anav for providing the data from CMIP5 and Zaichun Zhu for providing the LAI data. We are grateful to the scientists from NOAA/ESRL and the Scripps O_2 Program for making the invaluable data from the long-term measurements of CGR and O_2/N_2 available to the community.

W.L. is supported by the European Commission-funded project LUC4C (grant no. 603542). P.C. and S.Pe. acknowledge support from the European Research Council through Synergy grant ERC-2013-SyG-610028 "IMBALANCE-P". J.G.C. is supported by the Australian Climate Change Science Program, G.P. is supported by the Norwegian Research Council (236296), and J.P. is supported by the German Research Foundation's Emmy Noether Program.

Additional information

Supplementary information is available online.

Methods

Bayesian Estimation System. Each estimate of the 5-year mean carbon fluxes (and trends for Opt-B), called hereafter the "control variables" $\mathbf{x}$, is based on the update from a prior estimate of these variables $\mathbf{x}^{\mathbf{b}}$, using some observation-based estimates $\mathbf{y}^{\mathbf{o}}$ of the fluxes (and trends for Opt-B) that are connected to the control variables through the relationships H: $\mathbf{x}\rightarrow\mathbf{y}=H[\mathbf{x}]$. We follow a Bayesian statistical approach for this estimation. Assuming that the uncertainties in $\mathbf{x}^{\mathbf{b}}$ and $\mathbf{y}^{\mathbf{o}}$ are unbiased and Gaussian, characterized by the prior and observation uncertainty covariance matrices $\mathbf{B}$ and $\mathbf{R}$ respectively, and that H is linear (denoted as a matrix $\mathbf{H}$), the statistical estimate of $\mathbf{x}$, given $\mathbf{x}^{\mathbf{b}}$ and $\mathbf{y}^{\mathbf{o}}$, is unbiased and Gaussian, and the corresponding optimal estimate $\mathbf{x}^{\mathbf{a}}$ and uncertainty covariance matrix $\mathbf{A}$ are given (49) as:

$$\mathbf{A} = \left(\mathbf{B}^{-1} + \mathbf{H}^{\mathrm{T}}\mathbf{R}^{-1}\mathbf{H}\right)^{-1} \quad (1)$$

$$\mathbf{x}^{\mathrm{a}} = \mathbf{x}^{\mathrm{b}} + \mathbf{A}\mathbf{H}^{\mathrm{T}}\mathbf{R}^{-1}\left(\mathbf{y}^{0} - \mathbf{H}\mathbf{x}^{\mathrm{b}}\right) \quad (2)$$

where the superscripts T and "-1" are the transpose of a matrix and the inverse of a matrix, respectively.

In the optimization, Opt-A, we update the estimate of the mean fluxes of fossil fuel and cement emissions (F), ocean sink (O), land sink (B) and land-use change emissions (L) for each 5-year interval from 1980 to 2014 (Fig. 1 and Table S1). The observation vector contains estimates of 5-year mean global atmospheric growth rates of CO_2 (CGR, in Pg C yr^{-1}), atmospheric growth rates of O_2/N_2 (CGR-O_2, per meg unit), observation-based estimates of ocean sinks, land sinks, land-use change emissions and net land sink (B+L) (the data sources for these components of $\mathbf{y}^{\mathbf{o}}$ are summarized in Fig. 1 and provided in Table S2). The prior estimates for the different control variables are built with independent data sets so that there are no correlations between the prior uncertainties in the different control variables. The correlations between different 5-year intervals for CGR and O, and potential correlations between two data-driven estimates of O are estimated using the method in ref. (50). **H** in Opt-A is defined for each 5-year interval by:

$$\begin{array}{cccc} \mathbf{x} \rightarrow & \mathbf{y^o} & = & \mathbf{Hx} \\ \mathbf{H}: \begin{bmatrix} F \\ O \\ B \\ L \end{bmatrix} \rightarrow & \begin{bmatrix} CGR \\ CGR - O_2 \\ O \\ B \\ L \\ B + L \end{bmatrix} & = & \begin{bmatrix} F + O + B + L \\ \alpha_F F + \alpha_B (B + L) + Z_{O2} \\ O \\ B \\ L \\ B + L \end{bmatrix} \end{array} \quad (3)$$

where α_F, α_B and Z_{O2} are constant coefficients from ref. (15). The optimal estimate $\mathbf{x^a}$ discussed in the main text is computed by Eqs. (1) and (2).

In the optimization, Opt-B, we solve for the mean fluxes of F, O, fire emissions (FR), and for the linear relative trends of GPP (α) and TER (β) for each 5-year interval, as well as for the mean value of GPP (G_0) and TER (T_0) in the year 2005 (Fig. S5 and Table S1). The observation vector contains CGR, CGR-O_2, observation-based estimates of ocean sinks, net land sinks, fire emissions and linear relative trends of GPP (α) and TER (β). The linear relative trend of GPP (α) is not directly observable and we made the assumption that it is equal to the observable relative LAI trends from satellites (34–36). The relative trends of LAI (34–36), soil respiration (37) and G_0 (32, 33) are rather uncertain and sparse (Table S2). As for Opt-A, the prior covariance error matrix in Opt-B is also diagonal, while the observation covariance error matrix accounts for the potential correlations in the data-driven products (Table S1 and Table S2). The observation operator *H* is defined by the following relationship:

$$
\begin{array}{ccccc}
\mathbf{x} & \rightarrow & \mathbf{y^o} & = & H[\mathbf{x}] \\
H:\begin{bmatrix} F \\ O \\ G_0 \\ T_0 \\ \alpha \\ \beta \\ FR \end{bmatrix} & \rightarrow & \begin{bmatrix} CGR \\ CGR - O_2 \\ O \\ B+L \\ \alpha \\ GPP \\ \beta \\ FR \end{bmatrix} & = & \begin{bmatrix} F + O + GPP(G_0,\alpha) + TER\ (T_0,\beta) + FR \\ \alpha_F F + \alpha_B\left[GPP(G_0,\alpha) + TER(T_0,\beta) + FR\right] + Z_{O2} \\ O \\ GPP(G_0,\alpha) + TER(T_0,\beta) + FR \\ \alpha \\ GPP(G_0,\alpha) \\ \beta \\ FR \end{bmatrix}
\end{array} \tag{4}
$$

where GPP(G_0, α) and TER (T_0, β) for a given 5-year interval are functions of G_0 and T_0 with corresponding trends:

$$\mathrm{GPP_i}\left(G_0,\alpha\right) = G_0\left(1 + 3\alpha_i + \sum_{j=0}^{i-1} 5\times\alpha_j\right) \tag{5}$$

$$\mathrm{TER_i}\left(T_0,\beta\right) = T_0\left(1 + 3\beta_i + \sum_{j=0}^{i-1} 5\times\beta_j\right) \tag{6}$$

where the subscripts *i* and *j* are the number of 5-year intervals from the given 5-year to 2005. Eqs. (5) and (6) and, thus, the observation operator are not linear. However, assuming unbiased and Gaussian uncertainties in $\mathbf{x^b}$ and $\mathbf{y^o}$, the Bayesian inference indicates that the optimal estimate $\mathbf{x^a}$ of the control variables minimizes the following cost function (49):

$$J(\mathbf{x}) = \frac{1}{2}\left[\left(\mathbf{x}-\mathbf{x^b}\right)^T \mathbf{B}^{-1}\left(\mathbf{x}-\mathbf{x^b}\right) + \left(\mathbf{y^0} - H[\mathbf{x}]\right)^T \mathbf{R}^{-1}\left(\mathbf{y^0} - H[\mathbf{x}]\right)\right] \tag{7}$$

We minimize this cost function using a quasi-Newton iterative approach (49). At each iteration *n+1*, the operator *H* is linearized against the best estimate of the control variables $\mathbf{x}_n$ given by the previous iteration (or against $\mathbf{x^b}$ for the first iteration):

$$\mathbf{H}_{\mathbf{x}_n} = \left(\frac{\partial H}{\partial \mathbf{x}_n}\right)_{\mathbf{x}_n} \tag{8}$$

$$H[\mathbf{x}] \approx H[\mathbf{x}_\mathrm{n}] + \mathbf{H}_{\mathbf{x}_\mathrm{n}}(\mathbf{x} - \mathbf{x}_\mathrm{n}) \tag{9}$$

J is thus approximated by a quadratic function, whose minimum $\mathbf{x}_{n+1}$ is given by a revised version of Eqs. (1) and (2):

$$\mathbf{A}_{\mathrm{n+1}} = \left(\mathbf{B}^{-1} + \mathbf{H}_{\mathbf{x}_\mathrm{n}}^{\mathrm{T}} \mathbf{R}^{-1} \mathbf{H}_{\mathbf{x}_\mathrm{n}}\right)^{-1} \tag{10}$$

$$\mathbf{x}_{\mathrm{n+1}} = \mathbf{x}^{\mathbf{b}} + \mathbf{A}_{\mathrm{n+1}} \mathbf{H}_{\mathbf{x}_\mathrm{n}}^{\mathrm{T}} \mathbf{R}^{-1}\left(\mathbf{y}^{\mathbf{0}} - H\left[\mathbf{x}_{\mathbf{n}}\right] - \mathbf{H}_{\mathbf{x}_\mathrm{n}}\left(\mathbf{x}^{\mathbf{b}} - \mathbf{x}_{\mathbf{n}}\right)\right) \tag{11}$$

We continue to derive our approximation of $\mathbf{x}^\mathbf{a}$ until the series of $\mathbf{x}_n$ converges (relative difference between $\mathbf{x}_{n+1}$ and $\mathbf{x}_n$ within 1×10^{-5}). We approximate the uncertainty in this final estimate of the control variable using $\mathbf{A}_{n+1}$ (49).

Prior Data. To define the prior F, individual country data from four emission inventories (CDIAC (9), IEA (10), EDGAR (11) and BP (12)) are grouped into geographic regions as specified by the United Nations Statistics Division (http://unstats.un.org/unsd/methods/m49/m49regin.htm). Cement emissions from EDGAR are added into the IEA and BP data sets that do not include cement emissions. Uncertainties for each country (51) are used to create regional uncertainty distributions for each emission index using a bootstrapping method, with the uncertainties of the highest emitters in each region contributing the most to the uncertainty distributions. This effect is achieved by weighting the sampling probability (P_s) by the relative contribution of each country's emissions (E_C) to the total emissions within the region (E_R):

$$P_s = E_C / E_R \tag{12}$$

To constrain the temporal component of the emission errors, ten random samples are drawn from the corresponding regional uncertainty distribution for each country, producing ten random uncertainties for each country. These country-level uncertainties are used to constrain a random error time series covering 1980-2014, which is then run through an algorithm incorporating autocorrelated random noise, such that:

$$\varepsilon_{F(t)} = 0.95 \times \varepsilon_{F(t-1)} + \varepsilon_{(t)} \quad (13)$$

where emission error factors for any given year $\varepsilon_{F(t)}$ are correlated with the emission errors from the previous year $\varepsilon_{F(t-1)}$ by an autoregressive coefficient of 0.95 with $\varepsilon_{(t)}$ as random error. The autocorrelated time series are then multiplied and added to the fossil fuel emissions for each country, and subsequently 500 samples of global fossil fuel emissions are taken for each 5-year bin. The means and standard deviations of each bin for each inventory are calculated from these 500 samples. Additionally, the correlation in global uncertainty is calculated between 5-year bins and inventories to produce an error-covariance matrix. The maximum between the uncertainties calculated above and the standard deviations of the 5-year means across four emission inventories were adopted as the uncertainties of prior F.

Prior O values are set from the ocean biogeochemistry model values used in LQ15. Note that LQ15 adjusted their simulated O so as to match ocean observations during the decade of the 1990s and then used these bias-corrected ocean models outside this period. Here, for setting the prior O values, we consider simply the spread and the mean of ocean models without any adjustment.

Prior values of L and B are set from simulations in the TRENDY (v2) model intercomparison project (13). The simulations in TRENDY (v2) are up to 2012, and thus the priors for the period of 2010-2012 were used for 2013 to 2014. All the prior flux values are summarized in Table S1.

Correlations between Optimized Fluxes. Due to the very small uncertainties in CGR, there are relatively strong correlations between the optimized flux components related to CGR in Eq. (3) in the same period (Fig. S8a). To be specific, the fluxes B and O are negatively correlated, as are the fluxes F and L. Positive correlations can be seen between F and B, and between L and B. The correlations between fluxes in different periods can be attributed to the autocorrelations in observed CGR and O and the decadal mean observations used to constrain two consecutive 5-year periods. Similarly, the components related to CGR in Eq. (4) for Opt-B could also be correlated, because they are all constrained by CGR (Fig. S8b).

Sensitivity Tests. Sensitivity tests were conducted by doubling the uncertainty in prior F, testing prior F and its uncertainties from individual inventory data sets (IEA, EDGAR, CDIAC and BP), and using prior B and O from CMIP5 models (52) instead of TRENDY (v2) models and ocean carbon models from LQ15 in Opt-A (Fig. S3). The ocean sink is very robustly constrained in the optimization because of the sufficiency of constraining observational data, but the land sink is dependent on the prior F choice. By doubling the prior F uncertainties or replacing prior B and O with data from CMIP5, the means of all fluxes remain stable, although posterior uncertainties change slightly, emphasizing the robustness of this optimizing system. However, caution should be applied when deciding the means of prior F due to their relatively greater impacts on B and B+L.

Sensitivity tests for Opt-B were also performed, including: (a) using yearly GPP estimates during 1982-2011 from ref. (33) and removing LAI constraints as a proxy of the GPP relative trend (34–36); (b) only using the average GPP from MODIS (32) to constrain G_0; (c) only using the average GPP from ref. (33) to constrain G_0; (d) additionally using the 5-year mean GPP during 2000-2004, 2005-2009 and 2010-2014 from MODIS (32) to constrain the corresponding 5-year mean GPP; (e) setting prior relative trend of GPP (α) to 0; (f) setting prior trend of GPP (α) to 0 and removing LAI constraints to the relative trend of GPP (34–36); (g) removing the constraint from the trend of soil respiration (37); (h) setting prior trend of TER (β) to zero and removing the constraint from the trend of soil respiration (37); and (i) setting both prior trends of GPP (α) and TER (β) to 0 and removing LAI constraints (34–36). The optimized fluxes of F, O, B+L and FR are very stable in these sensitivity tests. The optimized mean values of GPP and TER vary (Fig.

S7) due to the large discrepancy between the GPP from MODIS and from ref. (33). However, the trends of GPP and TER are generally similar, but with slightly different scales (Fig. S7). This indicates that the patterns of GPP and TER are very robust and mutually controlled by the prior values, the LAI trend (34–36) and the soil respiration trend (37).

Trend Test. A Mann-Kendall statistical test was applied as a trend test. To remove autocorrelations, pre-whitening (53) was performed using the correlations between the posterior uncertainties (Fig. S8).

References

1. Wang X, et al. (2014) A two-fold increase of carbon cycle sensitivity to tropical temperature variations. *Nature* 506(7487):212–5.
2. Poulter B, et al. (2014) Contribution of semi-arid ecosystems to interannual variability of the global carbon cycle. *Nature* 509(7502):600–3.
3. Le Quéré C, et al. (2009) Trends in the sources and sinks of carbon dioxide. *Nat Geosci* 2(12):831–836.
4. Ghil M, Vautard R (1991) Interdecadal oscillations and the warming trend in global temperature time series. *Nature* 350(6316):324–327.
5. Raupach MR, et al. (2007) Global and regional drivers of accelerating CO2 emissions. *Proc Natl Acad Sci U S A* 104(24):10288–93.
6. Song X-P, Huang C, Saatchi SS, Hansen MC, Townshend JR (2015) Annual Carbon Emissions from Deforestation in the Amazon Basin between 2000 and 2010. *PLoS One* 10:e0126754.
7. Ciais P, et al. (2013) 2013: Carbon and Other Biogeochemical Cycles. *Clim Chang 2013 Phys Sci Basis Contrib Work Gr I to Fifth Assess Rep Intergov Panel Clim Chang*:465–570.
8. Le Quéré C, et al. (2015) Global carbon budget 2014. *Earth Syst Sci Data*:47–85.
9. Boden TA, Marland G, Andres RJ (2013) Global, regional, and national fossil-fuel CO□ emissions. *Carbon Dioxide Inf Anal Center, Oak Ridge Natl Lab USA Oak Ridge, TN Dep Energy*. doi:10.3334/CDIAC/00001.
10. International Energy Agency (2013) CO2 Emissions From Fuel Combustion Highlights. *IEA Stat*:158.
11. Olivier JGJ, Janssens-Maenhout G, Peters JAHW (2014) *Trends in global CO2 emissions: 2014 Report* (PBL Netherlands Environmental Assessment Agency Hague).
12. BP (2015) BP Statistical Review of World Energy 2015.
13. Sitch S, et al. (2015) Recent trends and drivers of regional sources and sinks of carbon dioxide. *Biogeosciences* 12(3):653–679.
14. NOAA/ESRL NOAA/ESRL calculation of global means. Available at: http://www.esrl.noaa.gov/gmd/ccgg/about/global_means.html [Accessed August 9, 2015].
15. Keeling RF, Manning a. C (2014) *Studies of Recent Changes in Atmospheric O2 Content* (Elsevier Ltd.). 2nd Ed. doi:10.1016/B978-0-08-095975-7.00420-4.
16. Landschützer P, Gruber N, Bakker DCE, Schuster U (2014) Recent variability of the global ocean carbon sink. *Global Biogeochem Cycles* 28(9):927–949.
17. Rödenbeck C, et al. (2014) Interannual sea–air CO_2 flux variability from an observation-driven ocean mixed-layer scheme. *Biogeosciences* 11(17):4599–4613.
18. Khatiwala S, Primeau F, Hall T (2009) Reconstruction of the history of anthropogenic CO(2) concentrations in the ocean. *Nature* 462(7271):346–9.
19. McNeil BI, Matear RJ, Key RM, Bullister JL, Sarmiento JL (2003) Anthropogenic CO2 uptake by the ocean based on the global chlorofluorocarbon data set. *Science* 299(5604):235–9.
20. Steinkamp K, Gruber N (2013) A joint atmosphere-ocean inversion for the estimation of seasonal carbon sources and sinks. *Global Biogeochem Cycles* 27(3):732–745.
21. Pan Y, et al. (2011) A large and persistent carbon sink in the world's forests. *Science* 333(6045):988–993.

22. Liu YY, et al. (2015) Recent reversal in loss of global terrestrial biomass. *Nat Clim Chang* 5(5):470–474.

23. Hansis E, Davis SJ, Pongratz J (2015) Relevance of methodological choices for accounting of land use change carbon fluxes. *Global Biogeochem Cycles* 29(8):1230–1246.

24. Houghton R a., et al. (2012) Carbon emissions from land use and land-cover change. *Biogeosciences* 9(12):5125–5142.

25. Piao SL, et al. (2012) The carbon budget of terrestrial ecosystems in East Asia over the last two decades. *Biogeosciences* 9(9):3571–3586.

26. Luyssaert S, et al. (2012) The European land and inland water CO_2, CO, CH_4 and N_2O balance between 2001 and 2005. *Biogeosciences* 9(8):3357–3380.

27. King AW, et al. (2015) North America's net terrestrial CO_2 exchange with the atmosphere 1990–2009. *Biogeosciences* 12(2):399–414.

28. Liu Z, et al. (2015) Reduced carbon emission estimates from fossil fuel combustion and cement production in China. *Nature* 524(7565):335–338.

29. Lucht W, et al. (2002) Climatic control of the high-latitude vegetation greening trend and Pinatubo effect. *Science* 296(5573):1687–9.

30. Mercado LM, et al. (2009) Impact of changes in diffuse radiation on the global land carbon sink. *Nature* 458(7241):1014–7.

31. Frölicher TL, Joos F, Raible CC, Sarmiento JL (2013) Atmospheric CO2 response to volcanic eruptions: The role of ENSO, season, and variability. *Global Biogeochem Cycles* 27(1):239–251.

32. Zhao M, Running SW, Nemani RR (2006) Sensitivity of Moderate Resolution Imaging Spectroradiometer (MODIS) terrestrial primary production to the accuracy of meteorological reanalyses. *J Geophys Res* 111(G1):G01002.

33. Jung M, et al. (2011) Global patterns of land-atmosphere fluxes of carbon dioxide, latent heat, and sensible heat derived from eddy covariance, satellite, and meteorological observations. *J Geophys Res* 116:G00J07.

34. Zhu Z, et al. (2013) Global Data Sets of Vegetation Leaf Area Index (LAI)3g and Fraction of Photosynthetically Active Radiation (FPAR)3g Derived from Global Inventory Modeling and Mapping Studies (GIMMS) Normalized Difference Vegetation Index (NDVI3g) for the Period 1981 to 2. *Remote Sens* 5(2):927–948.

35. Xiao Z, et al. (2014) Use of General Regression Neural Networks for Generating the GLASS Leaf Area Index Product From Time-Series MODIS Surface Reflectance. *IEEE Trans Geosci Remote Sens* 52(1):209–223.

36. Liu Y, Liu R, Chen JM (2012) Retrospective retrieval of long-term consistent global leaf area index (1981–2011) from combined AVHRR and MODIS data. *J Geophys Res* 117(G4):G04003.

37. Bond-Lamberty B, Thomson A (2010) Temperature-associated increases in the global soil respiration record. *Nature* 464(7288):579–82.

38. Giglio L, Randerson JT, van der Werf GR (2013) Analysis of daily, monthly, and annual burned area using the fourth-generation global fire emissions database (GFED4). *J Geophys Res Biogeosciences* 118(1):317–328.

39. Mieville A, et al. (2010) Emissions of gases and particles from biomass burning during the 20th century using satellite data and an historical reconstruction. *Atmos Environ* 44(11):1469–1477.

40. Schultz MG, et al. (2008) Global wildland fire emissions from 1960 to 2000. *Global Biogeochem Cycles* 22(2). doi:10.1029/2007GB003031.

41. Huang M, et al. (2015) Change in terrestrial ecosystem water-use efficiency over the last three decades. *Glob Chang Biol* 21(6):2366–78.

42. Gu L, et al. (2003) Response of a deciduous forest to the Mount Pinatubo eruption: enhanced photosynthesis. *Science* 299(5615):2035–8.

43. Cohen JL, Furtado JC, Barlow M, Alexeev VA, Cherry JE (2012) Asymmetric seasonal temperature trends. *Geophys Res Lett* 39(4). doi:10.1029/2011GL050582.

44. Tørseth K, et al. (2012) Introduction to the European Monitoring and Evaluation Programme (EMEP) and observed atmospheric composition change during 1972–2009. *Atmos Chem Phys* 12(12):5447–5481.

45. Davidson EA, et al. (2011) Excess nitrogen in the U.S. environment: Trends, risks, and solutions. *Issues Ecol* (15). Available at: https://pubs.er.usgs.gov/publication/70032270 [Accessed September 18, 2015].

46. Rayner PJ, et al. (2005) Two decades of terrestrial carbon fluxes from a carbon cycle data assimilation system (CCDAS). *Global Biogeochem Cycles* 19(2):n/a–n/a.

47. Peylin P, et al. (2016) A new step-wise Carbon Cycle Data Assimilation System using multiple data streams to constrain the simulated land surface carbon cycle. *Geosci Model Dev Discuss*:1–52.

48. United Nations (2015) Adoption of the Paris Agreement. *Conf Parties its twenty-first Sess* 21932(December):32.

49. Tarantola A (2005) *Inverse Problem Theory and Methods for Model Parameter Estimation* (SIAM).

50. Ballantyne AP, et al. (2015) Audit of the global carbon budget: estimate errors and their impact on uptake uncertainty. *Biogeosciences* 12(8):2565–2584.

51. Andres RJ, Boden TA, Higdon D (2014) A new evaluation of the uncertainty associated with CDIAC estimates of fossil fuel carbon dioxide emission. *Tellus B* 66. doi:10.3402/tellusb.v66.23616.

52. Anav A, et al. (2013) Evaluating the Land and Ocean Components of the Global Carbon Cycle in the CMIP5 Earth System Models. *J Clim* 26(18):6801–6843.

53. Yue S, Pilon P, Phinney B, Cavadias G (2002) The influence of autocorrelation on the ability to detect trend in hydrological series. *Hydrol Process* 16(9):1807–1829.

54. Jacobson AR, Fletcher SEM, Gruber N, Sarmiento JL, Gloor M (2007) A joint atmosphere-ocean inversion for surface fluxes of carbon dioxide: 1. Methods and global-scale fluxes. *Global Biogeochem Cycles* 21(1). doi:10.1029/2005GB002556.

55. Van Der Werf GR, et al. (2010) Global fire emissions and the contribution of deforestation, savanna, forest, agricultural, and peat fires (1997-2009). *Atmos Chem Phys* 10(23):11707–11735.

56. King AW, et al. (2007) *The North American Carbon Budget and Implications for the Global Carbon Cycle*.

57. SCHULZE ED, et al. (2010) The European carbon balance. Part 4: integration of carbon and other trace-gas fluxes. *Glob Chang Biol* 16(5):1451–1469.

58. Dolman AJ, et al. (2012) An estimate of the terrestrial carbon budget of Russia using inventory-based, eddy covariance and inversion methods. *Biogeosciences* 9(12):5323–5340.

59. Patra PK, et al. (2013) The carbon budget of South Asia. *Biogeosciences* 10:513–527.

60. Piao SL, et al. (2012) The carbon budget of terrestrial ecosystems in East Asia over the last two decades. *Biogeosciences* 9(9):3571–3586.

61. Gloor M, et al. (2012) The carbon balance of South America: a review of the status, decadal trends

and main determinants. *Biogeosciences* 9(12):5407–5430.

62. Valentini R, et al. (2014) A full greenhouse gases budget of Africa: synthesis, uncertainties, and vulnerabilities. *Biogeosciences* 11(2):381–407.

63. Haverd V, et al. (2013) The Australian terrestrial carbon budget. *Biogeosciences* 10(2):851–869.

Figure 1 The framework of Opt-A. The number of constraining data-streams and the specific data sources are marked on the right. The fluxes that are optimized are 5-year averages of F, O, B and L representing fossil fuel and cement emissions, ocean sink, land sink, and land-use change emissions, respectively. The observations used to constrain these fluxes are the five-year averaged growth rates of CO_2 and O_2/N_2 in the atmosphere, observations of O, B and the net land sink (B+L) from carbon measurements made in these two reservoirs, and inventory-based estimates of L. In this framework, the CO_2 growth rate constrains the sum of all the fluxes. The O_2/N_2 growth rate allows us to separate O and B+L and bring some constraint on F as well.

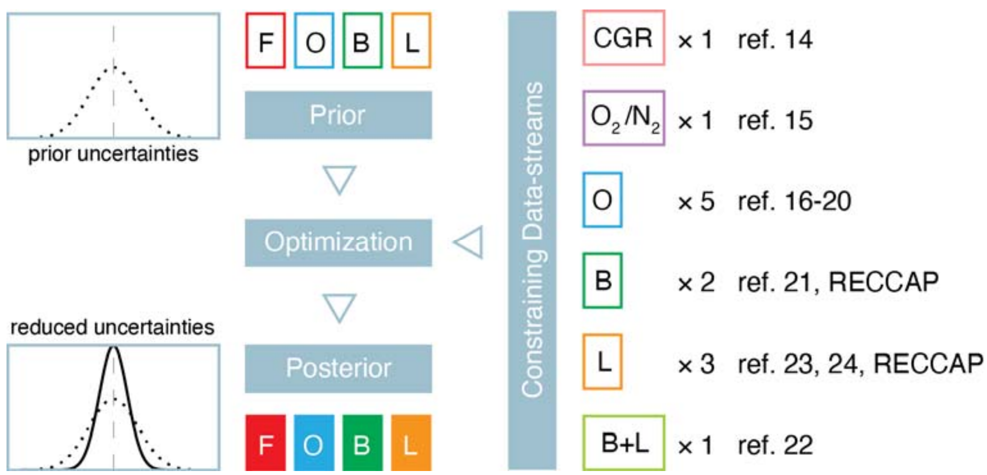

Figure 2 (**a**) The fossil fuel and cement emissions (F), (**b**) ocean sink (O) and (**c**) net land flux (B+L), and (**d**) land sink (B) and land-use change emissions (L) from prior knowledge, Opt-A and LQ15. All the fluxes are 5-year means in each period. The error bars represent the 1-σ uncertainties.

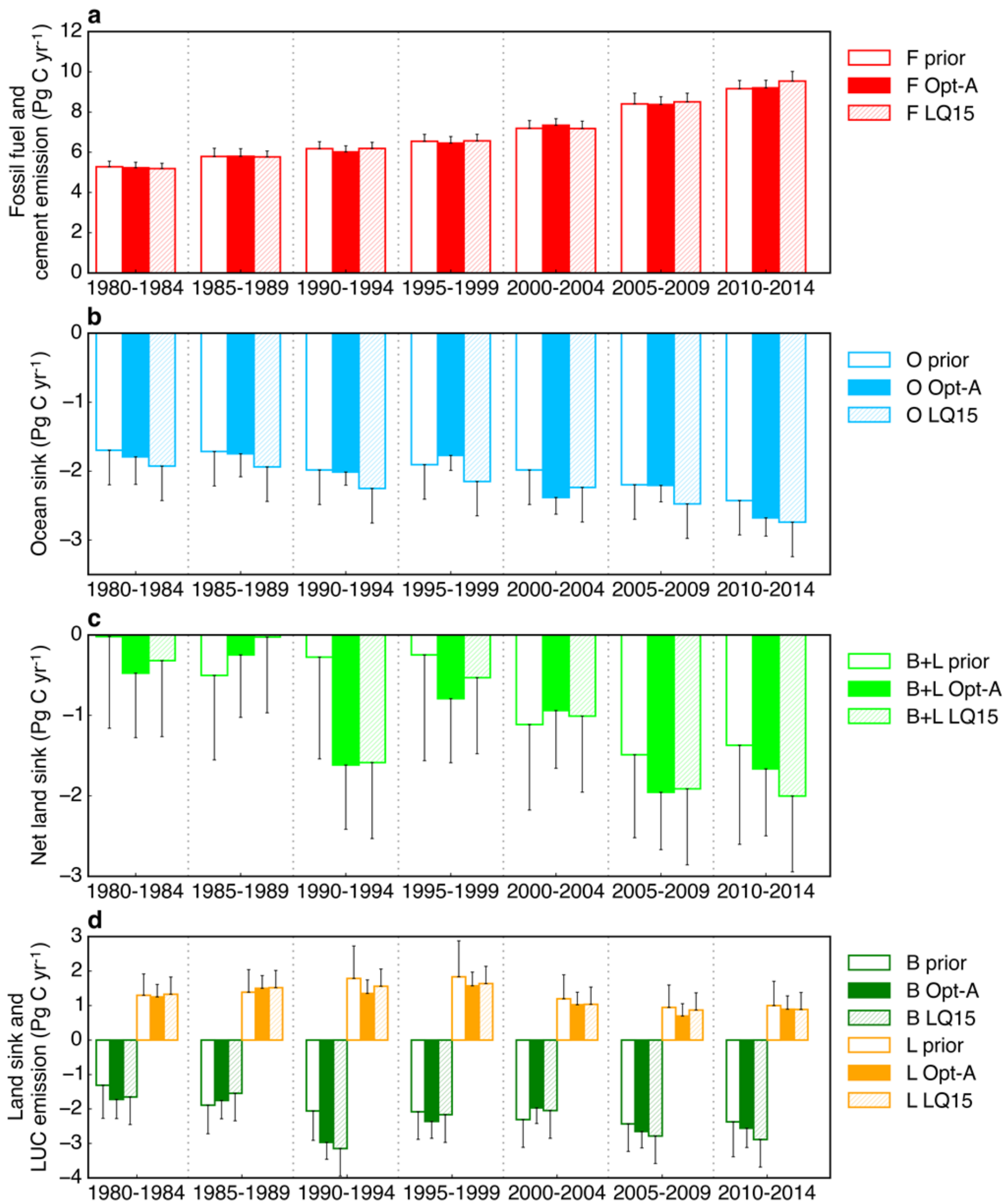

Figure 3 (**a**) The prior and the optimized gross primary production (GPP, shown as reversed sign) and terrestrial ecosystem respiration (TER) and (**b**) the prior and the optimized fire emissions (FR) from Opt-B. The error bars represent the 1-σ uncertainties. Uncertainties in the prior GPP and TER are not shown because of their large size (about 35 Pg C yr^{-1}).

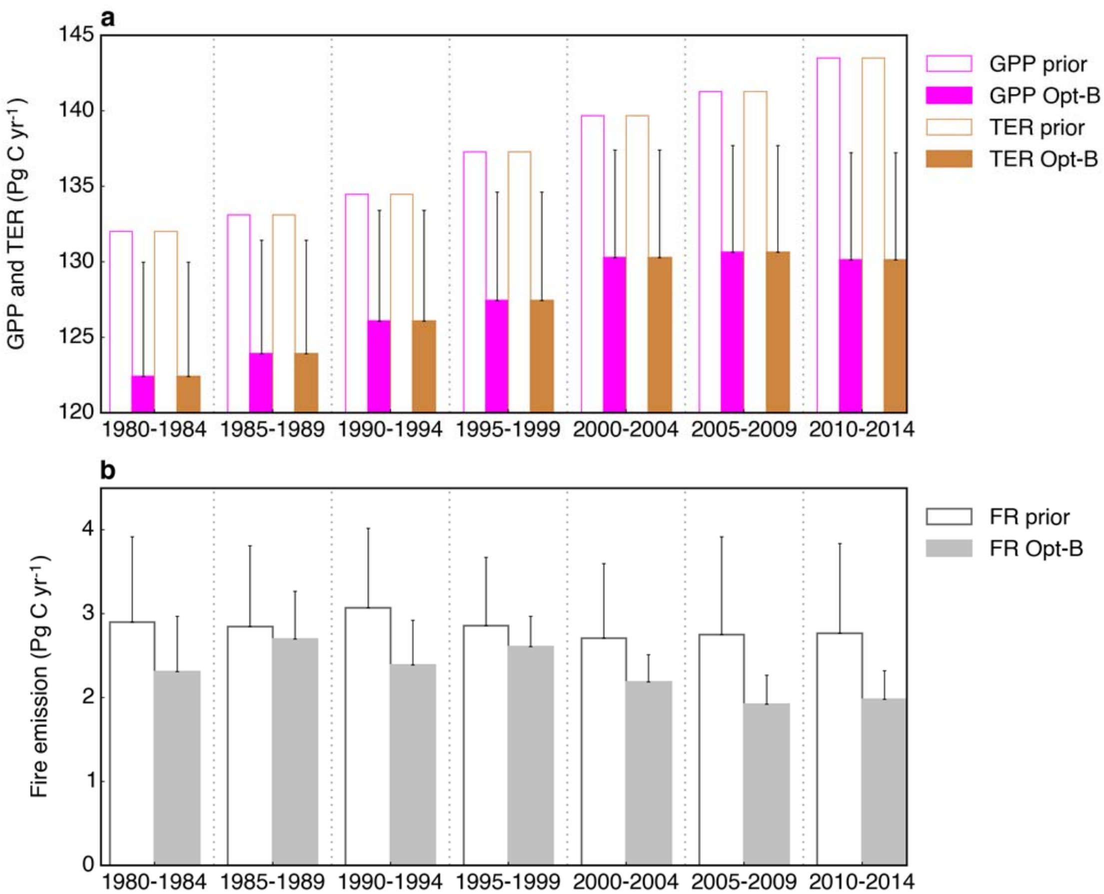

Supporting information

Table S1 Prior and optimized values and uncertainties.

		80-84	85-89	90-94	95-99	00-04	05-09	10-14
prior	F (Pg C yr^{-1})	5.27±0.28	5.79±0.41	6.18±0.35	6.55±0.35	7.19±0.39	8.40±0.53	9.16±0.41
	O (Pg C yr^{-1})	-1.70±0.50	-1.71±0.50	-1.98±0.50	-1.91±0.50	-1.98±0.50	-2.20±0.50	-2.43±0.50
	B (Pg C yr^{-1})	-1.31±0.95	-1.89±0.83	-2.06±0.85	-2.08±0.80	-2.31±0.80	-2.43±0.80	-2.37±1.01
	L (Pg C yr^{-1})	1.30±0.62	1.39±0.65	1.78±0.94	1.83±1.04	1.20±0.70	0.94±0.65	1.00±0.70
	α (Pg C yr^{-2})	0.08±0.56	0.61±0.52	-0.19±0.50	1.07±0.13	-0.11±0.55	0.37±0.12	-0.27±0.78
	β (Pg C yr^{-2})	-0.06±0.28	0.55±0.14	-0.17±0.56	0.89±0.42	-0.23±0.24	0.13±0.11	-0.36±0.01
	G_0 (Pg C yr^{-1})						-140.27±36.58	
	T_0 (Pg C yr^{-1})						129.54±44.21	
	FR (Pg C yr^{-1})	2.90±1.02	2.85±0.96	3.07±0.95	2.86±0.81	2.71±0.89	2.75±1.17	2.77±1.07
Opt-A	F (Pg C yr^{-1})	5.22±0.27	5.77±0.38	5.98±0.31	6.45±0.32	7.32±0.32	8.28±0.38	9.15±0.37
	O (Pg C yr^{-1})	-1.82±0.40	-1.76±0.33	-2.02±0.19	-1.77±0.22	-2.39±0.24	-2.23±0.24	-2.70±0.26
	B (Pg C yr^{-1})	-1.86±0.53	-1.83±0.52	-3.10±0.45	-2.34±0.44	-2.03±0.43	-2.80±0.45	-2.83±0.50
	L ((Pg C yr^{-1})	1.43±0.29	1.63±0.30	1.53±0.31	1.55±0.29	1.13±0.27	0.96±0.22	1.24±0.19
	B+L (Pg C yr^{-1})	-0.43±0.70	-0.20±0.69	-1.57±0.67	-0.79±0.64	-0.90±0.59	-1.83±0.56	-1.59±0.59
Opt-B	F (Pg C yr^{-1})	5.24±0.27	5.92±0.40	6.08±0.32	6.54±0.33	7.44±0.32	8.48±0.42	9.33±0.39
	O (Pg C yr^{-1})	-1.77±0.42	-1.66±0.34	-2.03±0.19	-1.74±0.22	-2.32±0.24	-2.15±0.24	-2.60±0.27
	α (Pg C yr^{-2})	-0.08±0.41	0.88±0.33	-0.25±0.39	1.04±0.12	-0.13±0.30	0.36±0.11	-0.79±0.43
	β (Pg C yr^{-2})	0.03±0.27	0.53±0.13	-0.16±0.40	1.18±0.28	-0.23±0.23	0.14±0.11	-0.36±0.01
	G_0 (Pg C yr^{-1})						-129.91±7.05	
	T_0 (Pg C yr^{-1})						126.29±7.08	
	FR (Pg C yr^{-1})	2.31±0.66	2.70±0.57	2.39±0.53	2.61±0.36	2.19±0.32	1.92±0.35	1.98±0.34
	GPP (Pg C yr^{-1})	-122.42±7.56	-123.93±7.49	-126.09±7.32	-127.42±7.21	-130.29±7.11	-130.63±7.05	-130.13±7.10
	TER (Pg C yr^{-1}))	119.59±7.53	120.75±7.47	122.02±7.33	123.89±7.21	126.98±7.10	126.56±7.08	126.26±7.08
	B+L (Pg C yr^{-1})	-0.52±0.54	-0.49±0.54	-1.69±0.41	-0.92±0.42	-1.11±0.41	-2.14±0.50	-1.89±0.51

Table S2 Sources and values of different constraining data-streams used in Opt-A and Opt-B. The blue and orange shades indicate the length of time covered.

	80-84	85-89	90-94	95-99	00-04	05-09	10-14	Opt-A	Opt-B	Reference
CGR (Pg C yr^{-1})	2.94±0.22	3.81±0.22	2.35±0.18	3.89±0.18	3.93±0.16	4.12±0.16	4.80±0.16	x	x	Means are from NOAA (14), and uncertainties are from “Table 1” in Ballantyne et al. (50).
O (Pg C yr^{-1})	-1.79±1.07	-1.85±1.07	-1.88±1.07	-1.53±1.07	-1.59±1.07	-2.02±1.07	-2.28±1.07	x	x	Values from Landschützer et al. (16) are added to an outgassing of 0.45 Pg C yr^{-1} and the corresponding uncertainties from Jacobson et al. (54).
O (Pg C yr^{-1})		-1.82±0.68	-2.03±0.68	-1.68±0.68	-1.76±0.68	-1.56±0.68	-2.39±0.68	x	x	Values from Rödenbeck et al. (17) are added to an outgassing of 0.45 Pg C yr^{-1} and the corresponding uncertainties from Jacobson et al. (54).
O (Pg C yr^{-1})			-2.00±0.40					x	x	Means and uncertainties are from McNeil et al. (19) to constrain O from 1990 to 1999.
O(Pg C yr^{-1})			-1.80±0.20					x	x	Means and uncertainties are from Steinkamp and Gruber (20) to constrain O from 1990 to 1999.
O (Pg C yr^{-1})			-1.91±0.60	-2.05±0.60				x	x	Means and uncertainties are from Khatiwala et al. (18).
B (Pg C yr^{-1})			-2.50±1.08		-2.30±1.12			x		Means are from Pan et al. (21). Given that B here only accounts for the carbon sink in global established forests, the uncertainties of global residuals in “Table 3” from Pan et al. (21) are also included, which may represent the uncertainty of land carbon sinks from other ecosystems like grassland.
B (Pg C yr^{-1})					-1.70±0.57			x		RECCAP (see **Table S3**)
L (Pg C yr^{-1})					1.00±0.19			x		RECCAP (see **Table S3**)
L (Pg C yr^{-1})	1.33±0.50	1.52±0.50	1.56±0.50	1.64±0.50	1.04±0.50	0.87±0.50	0.88±0.50	x		Means and uncertainties are from the bookkeeping model by Houghton et al. (24), which is also used in the global carbon budget from Le Quéré et al. (8).
L (Pg C yr^{-1})	1.76±0.49	1.89±0.52	1.82±0.50	1.54±0.43	1.27±0.40	1.13±0.28	1.36±0.22	x		Means and uncertainties are from the BLUE model by Hansis et al. (23). The uncertainties refer to the difference to the alternative estimate.
O_2/N_2[a] (per meg unit)			-6.10±0.22	-7.37±0.69	-8.89±0.30	-9.15±0.35	-10.64±0.37	x	x	Data are from Scripps O_2 program (http://scrippso2.ucsd.edu/), and the weighted average of data from stations of Alert, La Jolla and Cape Grim are taken as the global means as in Keeling et al. (15). The standard deviations across data from these stations are used as uncertainties.
B+L[b] (Pg C yr^{-1})					-1.82±0.55			x	x	Values are from Liu et al. (22). They estimated the aboveground biomass carbon from Vegetation Optical Depth, extrapolated to the total biomass by the ratios between aboveground and belowground biomass in

									different regions, and then calculated the total carbon (including litter and soil carbon) trend based on the ratios between total carbon and total biomass.
LAI trend[c]	0.04±0.02	0.08±0.10	-1.66±0.48	-0.06±0.24	0.26±0.18	-0.04±0.05		x	The trend of LAI is calculated from the average of global mean LAI from 3 datasets: GIMMS LAI3G (Zhu et al. (34)), GLASS LAI (Xiao et al. (35)) and GLOBMAP LAI (Liu et al. (36)). The errors in the linear trend regression are taken as uncertainties.
β (Pg C yr^{-2})			0.10±0.49					x	An assumed linear trend of soil respiration from 1989 to 2008 is calculated from Bond-Lamberty and Thomson. (37). Note that the trend of soil respiration here is used as a proxy of the global TER trend, and the autotrophic respiration is omitted. The value of soil respiration is not used to constrain TER, because of the omission of autotrophic respiration.
GPP[d] (Pg C yr^{-1})					-110.79±21.17			x	GPP values are from MODIS by Zhao et al. (32). The average of global yearly GPP between 2001 and 2009 is used here. The uncertainties are estimated from the variations between different meteorological data required in the MODIS GPP calculation by Zhao et al. (32).
GPP[e] (Pg C yr^{-1})					-131.88±7.76			x	GPP values are from the upscaling of FLUXNET by Jung et al. (33). The average of global yearly mean GPP between 2001 and 2009 is used here. The uncertainties refer to the standard deviation across different model trees in Jung et al. (33).
FR (Pg C yr^{-1})				2.50±0.50	1.97±0.39	1.92±0.38	1.83±0.37	x	Means are from GFED4 by Giglio et al. (38), and uncertainties of 20% are assumed, as by van der Werf et al. (55).
FR (Pg C yr^{-1})	2.40±0.96		2.58±1.03	2.78±1.11	2.53±1.01			x	Means are from GICC data set, and the uncertainties are set as 40% based on the uncertainties on burned areas in Mieville et al. (39).
FR (Pg C yr^{-1})	2.14±1.07	1.84±0.92	2.42±1.21	2.35±1.17				x	Means are from RETRO data set, and the estimated uncertainties of 50% by Shultz et al. (40) is adopted here.

[a] The relationship of $\Delta O_2 = -\alpha_F F + \alpha_B(B+L) + Z_{O2}$ from Keeling et al. (15) is used.

[b] B+L is corresponding to B+L in Opt-A and is corresponding to $(G_0+\alpha t) + (T_0+\beta t)$ + FR in Opt-B.

[c] The relative trend of LAI is used to constrain the relative trend of GPP.

[d] The average of yearly GPP values between 2001 and 2011 (the overlapped period of GPP from FLUXNET) is used to constrain G_0.

[e] The average of yearly GPP values from 2001 to 2011 (the overlapped period of GPP from MODIS) is used to constrain G_0.

Table S3 The estimates of B and L from Regional Carbon Cycle Assessment and Processes (RECCAP) international research project. In brief, the observed carbon fluxes in the nine regions were evaluated and summed to give the global fluxes. The net ecosystem exchange (NEE) calculated from the mass balance of the emissions and outgassing of carbon to the atmosphere, net primary production (NPP), and soil heterotrophic respiration (SHR) is taken as B in this study. Negative values indicate a flux from the atmosphere to the land.

region	flux	period	Mean (Tg C yr^{-1})	Uncertainty (Tg C yr^{-1})	Reference
North America	L	2000s	-130	60	King et al. (56)
	B	2000-2009	-418	288	Mass balance
Europe	L	2003-2007	-2	1	Schulze et al. (57)
	B	2000-2007	-234	166	Mass balance
Russia	L	1990-2006	-34	2	Dolman et al. (58)
	B	2007-2009	-600	224	Mass balance
South Asia	L	2000-2009	-14	50	Patra et al. (59)
	B	2000-2009	-86	34	Mass balance
East Asia	L	2000-2009	-13	29	Piao et al. (60)
	B	2000-2009	-256	35	Mass balance
Southeast Asia	L	undefined	59	12	Liu et al. (22) only over LUC affected grid cells
	B	undefined	-97	186	Mass balance
South America	L	1990-2012	525	130	Gloor et al. (61) “Table 12”
	B	2000-2009	11	284	Mass balance
Africa	L	1990-2009	510	100	Valentini et al. (62) “Table 11”
	B	2000-2007	12	292	Mass balance
Australia	L	1990-2011	18	7	Haverd et al. (63)
	B	1990-2011	-71	36	Mass balance
Globe	L	2000-2009	919	184	sum
	B	2000-2009	-1740	604	sum

Figure S1 The values and uncertainties of ocean sinks (O), land sinks (B) and land-use change (LUC) emissions (L) in different data-streams. The dashed lines indicate the period covered.

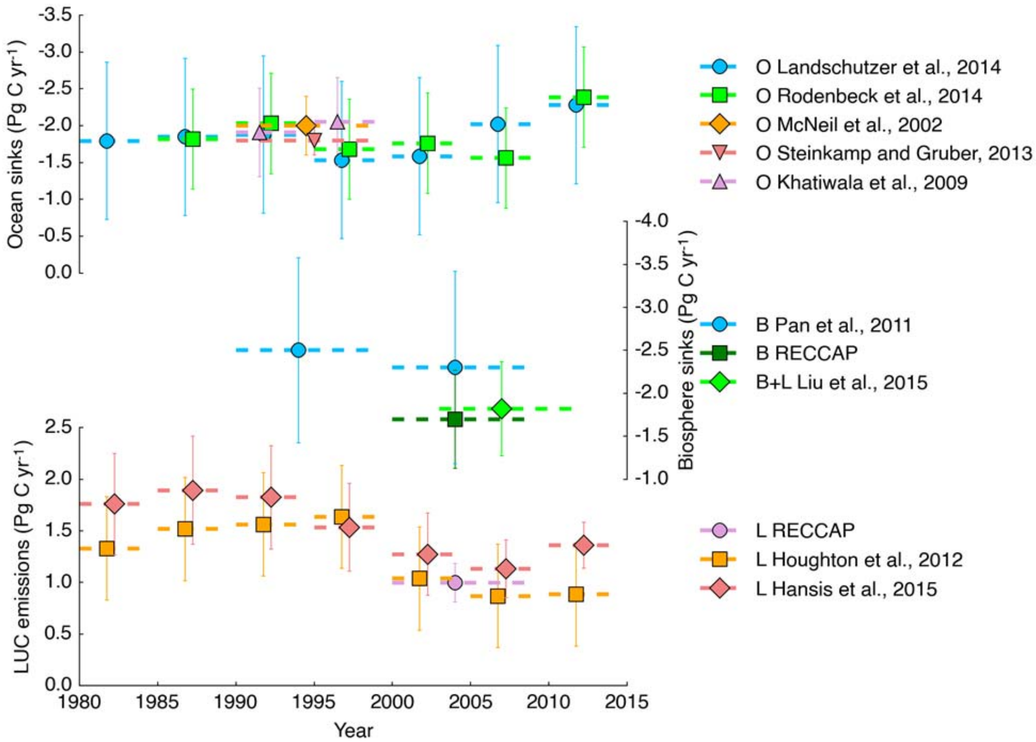

Figure S2 The temporal trend of ocean sink (O), land sink (B), land-use change emissions (L) and net land flux (B+L) from Opt-A and LQ15.

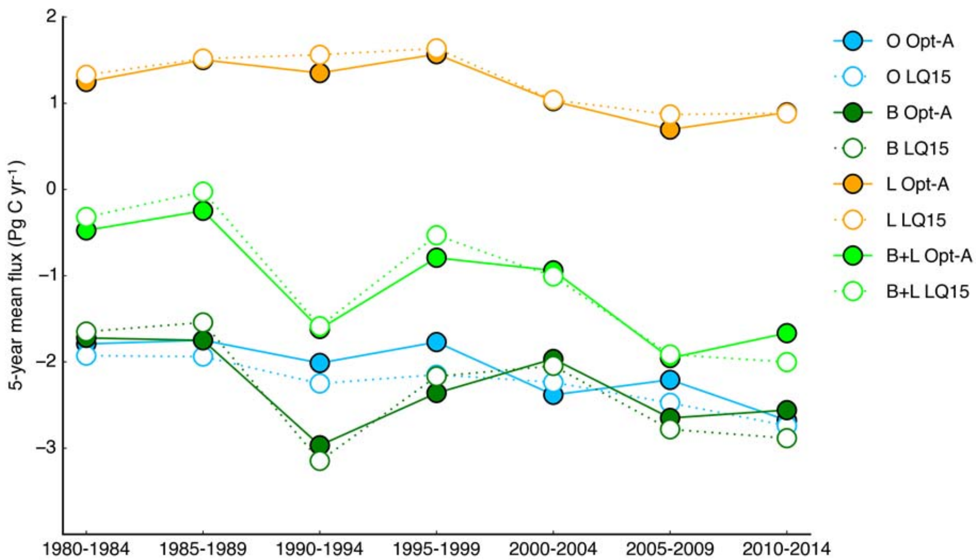

Figure S3 The fluxes of fossil fuel and cement (F), and land-use change (L) emissions, ocean (O) and land (B) sink, and net land sink (B+L) using different prior data. The bars around each flux in each period from left to right represent Opt-A, double prior uncertainties, prior F from IEA, prior F from EDGAR, prior F from CDIAC, prior F from BP and prior B and O from CMIP5, respectively.

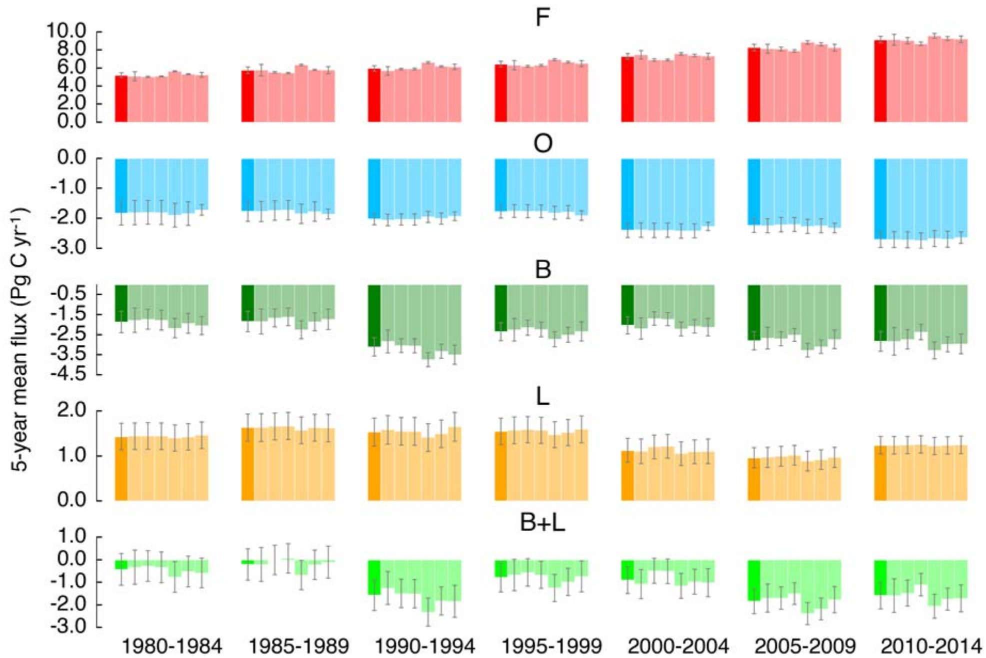

Figure S4 The partitioning of global total emissions (fossil fuel and cement emissions and land-use change emissions, F+L) into atmosphere, ocean (O) and biosphere (B, background shade). The markers are absolute absorbed fractions and uncertainties in ocean (blue circles) and biosphere (green squares).

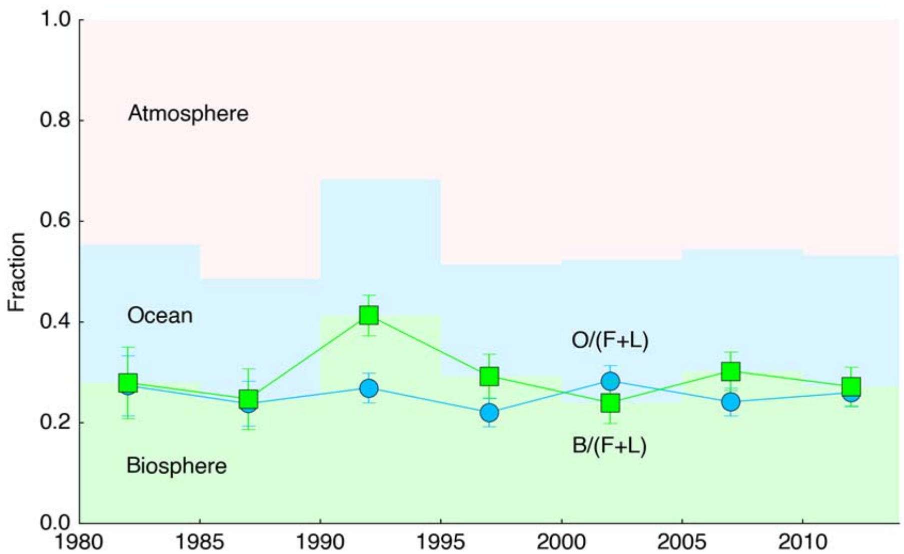

Figure S5 The framework of Opt-B. The number of data-streams is marked on the right.

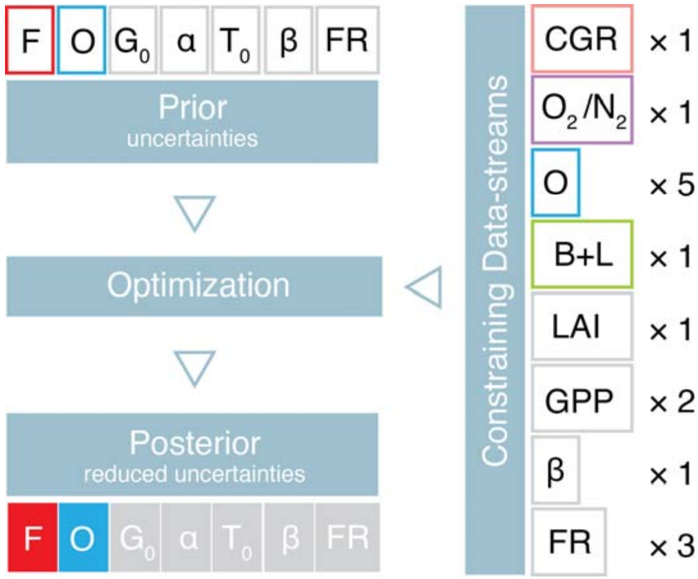

Figure S6 (**a**) The fossil fuel and cement emissions (F) and (**b**) the ocean sink (O) and net land flux (B+L) from prior knowledge, Opt-A and Opt-B. All the fluxes are 5-year means over each period.

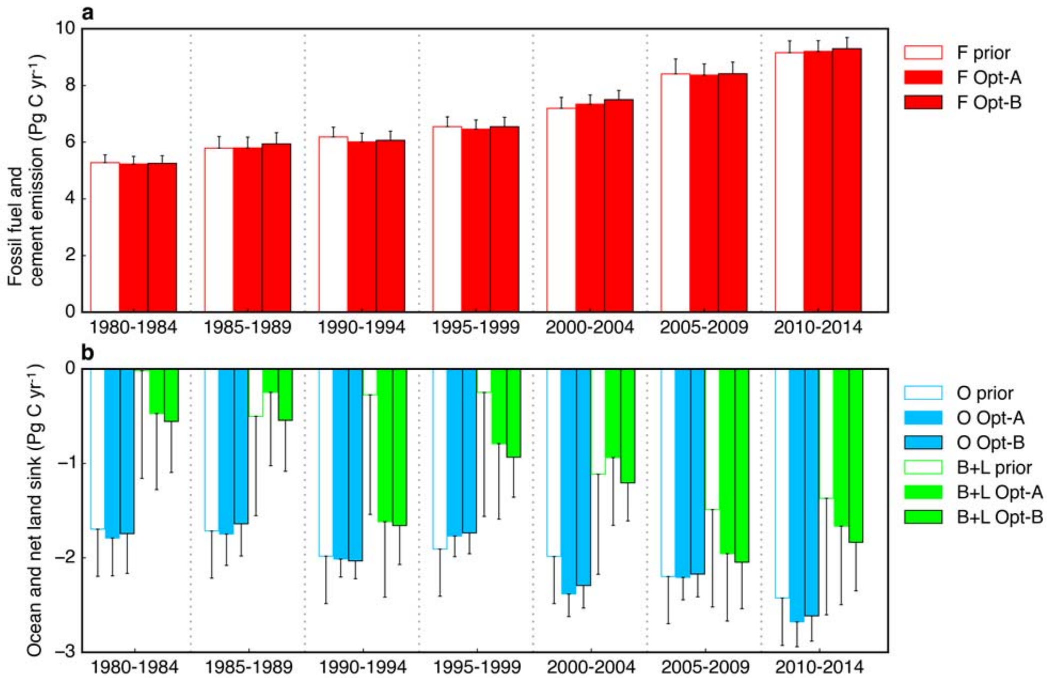

Figure S7 The optimized gross primary production (GPP, shown as reversed sign) and terrestrial ecosystem respiration (TER) in the sensitivity tests for Opt-B. The shaded areas represent their uncertainties. The differences between sensitivity tests and Opt-B are: (a) using yearly GPP estimates during 1982-2011 from ref. (33) and removing LAI constraints as a proxy of the GPP relative trend(34–36); (b) only using the average GPP from MODIS(32) to constrain G_0; (c) only using the average GPP from ref. (33) to constrain G_0; (d) additionally using the 5-year mean GPP during 2000-2004, 2005-2009 and 2010-2014 from MODIS(32) to constrain the corresponding 5-year mean GPP; (e) setting prior relative trend of GPP (α) to zero; (f) setting prior trend of GPP (α) to 0 and removing LAI constraints to the relative trend of GPP(34–36); (g) removing the constraint from the trend of soil respiration(37); (h) setting prior trend of TER (β) to zero and removing the constraint from the trend of soil respiration(37); and (i) setting both prior trends of GPP (α) and TER (β) to 0 and removing LAI constraints(34–36).

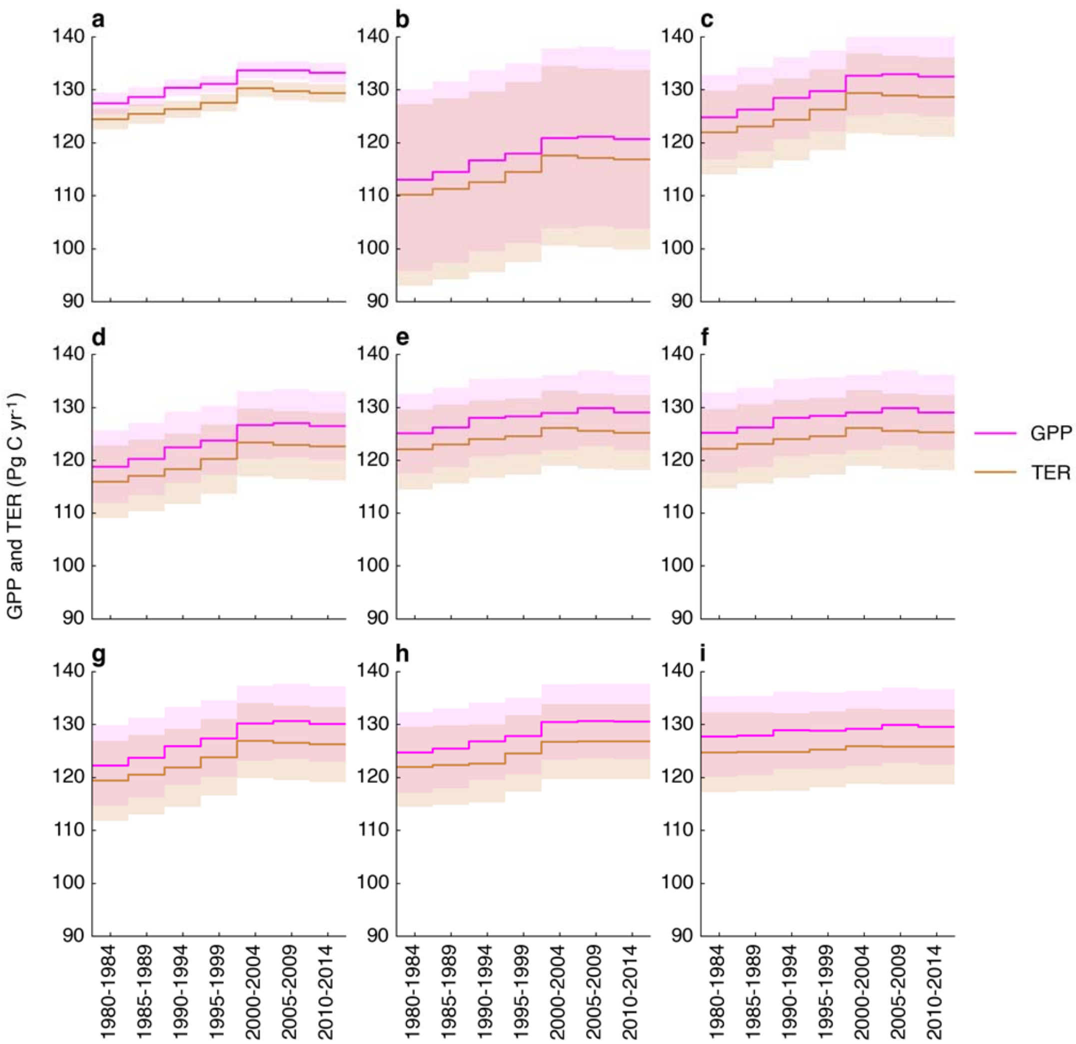

Figure S8 Correlations between the posterior uncertainties in (**a**) Opt-A and (**b**) Opt-B. The subscripts 1 to 7 represent the 5-year periods from 1980-1984 to 2010-2014 in sequence.